Available online at www.sciencedirect.com

ScienceDirect

Acta Materialia 92 (2015) 220–232

Acta MATERIALIA

www.elsevier.com/locate/actamat

A hierarchical microstructure due to chemical ordering in the bcc lattice: Early stages of formation in a ferritic Fe–Al–Cr–Ni–Ti alloy

C.H. Liebscher,[a,b,*] V.R. Radmilović,[b,c] U. Dahmen,[b] N.Q. Vo,[d] D.C. Dunand,[d] M. Asta[a] and G. Ghosh[d]

[a]*Department of Materials Science and Engineering, University of California, Berkeley, CA 94720, USA*
[b]*National Center for Electron Microscopy, Lawrence Berkeley National Laboratory, Berkeley, CA 94720, USA*
[c]*Nanotechnology and Functional Materials Center, Faculty of Technology and Metallurgy, University of Belgrade and Serbian Academy of Sciences and Arts, 11120 Belgrade, Serbia*
[d]*Department of Materials Science and Engineering, Northwestern University, Evanston, IL 60208, USA*

Received 28 January 2015; revised 16 March 2015; accepted 26 March 2015
Available online 22 April 2015

Abstract—A hierarchical microstructure is obtained in an alloy with composition Fe–8.1Al–12.2Cr–1.9Mo–18.2Ni–2.0Ti (wt.%) processed by melt-spinning. The evolution of the precipitation pathways is investigated using transmission electron microscopy (TEM) techniques, atom probe tomography (APT) and first-principles thermodynamic calculations. As-solidified ribbons exhibit a random dispersion of B2-ordered precipitates (NiAl-type) in an Fe-based matrix. Subsequent aging at 700 °C yields nucleation and growth of the $L2_1$-phase (Ni_2TiAl-type) within the primary B2-precipitates, leading to a microstructure exhibiting three types of hierarchy: (i) a structural hierarchy due to chemical ordering, with a chemically disordered matrix of bcc-Fe (A2), the nearest-neighbor (NN) ordered B2-precipitates (NiAl-type) and the next nearest-neighbor (NNN) ordered $L2_1$-precipitates (Ni_2TiAl-type) within B2, (ii) a dimensional hierarchy with a continuous bcc-Fe matrix, coherently embedded B2-precipitates, with a size range of 60–200 nm and the coherent precipitate substructure, with $L2_1$-phase and dimensions of 15–20 nm. (iii) A spatial hierarchy where B2-precipitates are embedded in the bcc-Fe matrix and $L2_1$-precipitates nucleate and grow only within B2-precipitates. In addition, it is verified that the interface between B2 and $L2_1$ is coherent and adopts a diffuse structural profile. Monte-Carlo simulations reproduce these observations and it is found that interface energies of B2 and $L2_1$ reduce from 50 mJ/m^2 at 0 K to 11 mJ/m^2 at 973 K. Kinetic-Monte-Carlo simulations support the interpretation of the experimental results that the $L2_1$ nucleates within the B2 phase.
© 2015 Acta Materialia Inc. Published by Elsevier Ltd. All rights reserved.

Keywords: Ferritic alloys; Precipitation hardening; Heusler alloy; Transmission electron microscopy; First-principles Monte-Carlo simulations

1. Introduction

Recently, precipitation strengthened alloys based on the Fe–Al–Cr–Ni system have been the subject of several investigations focused on structure–properties relations in the context of developing ferritic materials capable of applications at higher operating temperature [1–3]. The microstructure of these ferritic alloys is composed of a continuous bcc-Fe matrix and B2-NiAl primary precipitates [3–8]. It has been shown recently that through the addition of Ti to such alloys, single phase $L2_1$-Ni_2TiAl or two-phase $L2_1$-Ni_2TiAl/B2-NiAl precipitates can be formed coherently in the Fe-matrix [2,9].

The phase equilibria characterizing this alloy system thus allow, through relatively simple solid-state aging, a separation of microstructure into two sub-systems. The basic components are the bcc-Fe matrix and primary precipitates. The volume fraction of the primary precipitates can be controlled primarily through the Ni and Al content [8]. Ti partitions to the precipitate phase [2,9] and thus enables a two-phase decomposition within the primary precipitates, to a degree that can be controlled by the Ti content. Specifically, the quasi-binary NiAl–NiTi system is characterized by a two-phase region, bounding the B2 (NiAl) and $L2_1$ (Ni_2TiAl) phases, which are linked by ordering on the Al-sublattice of the B2-NiAl structure [10].

The microstructure of the Ti-containing Fe–Al–Cr–Ni alloys can thus be described as hierarchical, characterized by the relative chemical ordering, spatial dimensions of the phases and their spatial distribution. The Fe-base matrix is continuous and is therefore characterized by the largest length scale. The primary precipitates are described by a smaller length scale, which is further subdivided by the precipitate sub-structure at the lowest tier of the hierarchical structure. The matrix is chemically disordered (Fig. 1a) where the major alloying elements Fe, Cr, Ni and Al are distributed with equal probability over the bcc lattice sites.

* Corresponding author at: Max-Planck-Institut für Eisenforschung, 40237 Düsseldorf, Germany.

http://dx.doi.org/10.1016/j.actamat.2015.03.043
1359-6462/© 2015 Acta Materialia Inc. Published by Elsevier Ltd. All rights reserved.

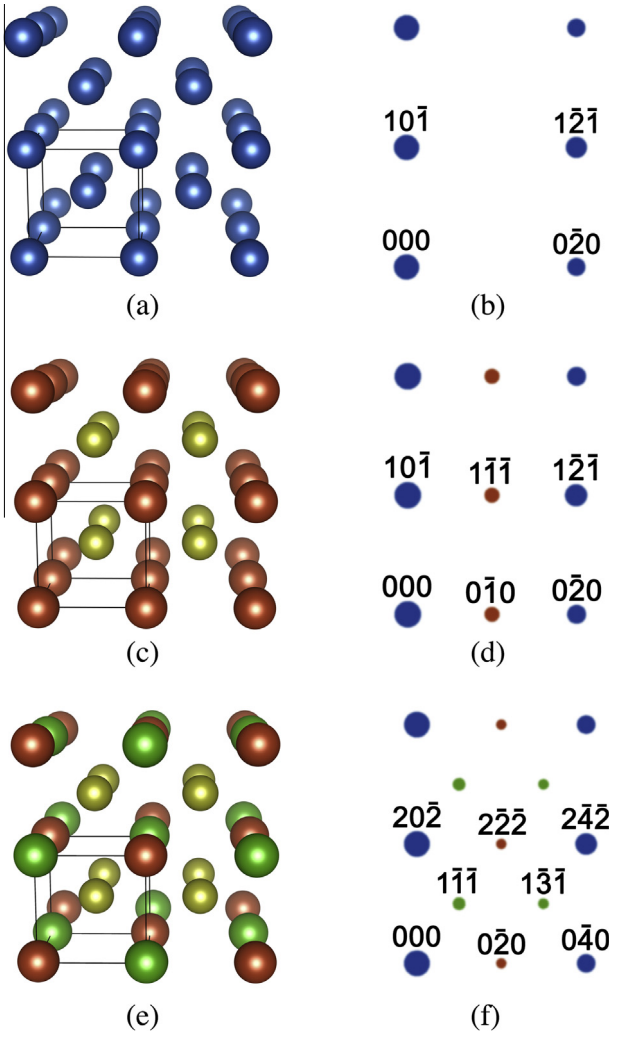

Fig. 1. Crystal structures and schematic quadrants of the [1 0 1] electron diffraction patterns for the A2-Fe matrix (a) and (b), B2-NiAl (c) and (d) and $L2_1$-Ni_2TiAl (e) and (f). For each crystal structure eight bcc unit cells are displayed and the cube edges of a single bcc unit cell are outlined. Fe atoms are colored in blue, Ni atoms in yellow, Al atoms in red and Ti atoms in green.(For interpretation of the references to colour in this figure legend, the reader is referred to the web version of this article.)

The precipitates and precipitate sub-structure are chemically ordered phases exhibiting either two, i.e., nearest-neighbor (NN, B2-NiAl, Fig. 1c), or three, i.e., next nearest-neighbor (NNN, $L2_1$-Ni_2TiAl, Fig. 1e), distinct sublattices. These phases can be considered as being built from one and two families of ordering waves, respectively [11–13].

In a previous paper we demonstrated the formation of two-phase precipitates in an Fe–Al–Cr–Ni–Ti based alloy with Ti concentrations of 4 wt.% [9]. In this alloy it was shown that the host precipitate is $L2_1$-Ni_2TiAl and B2-NiAl zones are formed within the precipitate in the course of the aging heat treatment. The phase-transformation mechanism resulting in the two-phase precipitate microstructure has been argued to be influenced by a wetting of B2-NiAl on antiphase boundaries in the $L2_1$-precipitate.

In this paper we present a detailed characterization of the early stages of microstructural evolution in a similar ferritic alloy with a lower Ti concentration of 2 wt.% Ti. Again, solid-state aging leads to a hierarchical microstructure, but initially with the primary precipitate phase being B2-NiAl, and later with $L2_1$-Ni_2TiAl precipitates nucleating and growing within the former. The emphasis of the present study is to elucidate the phase transformation pathway for this lower Ti concentration sample through a combined experimental and computational study. The goal is to develop a comprehensive picture of the influence of Ti additions on the microstructure in precipitation strengthened ferritic alloys, to aid further design of creep resistant alloys.

To investigate the phase separation sequence in the early stages of aging at 700 °C, we use transmission electron microscopy (TEM) techniques such as dark-field imaging, high resolution scanning TEM (STEM), energy dispersive X-ray spectroscopy (EDS), energy filtered TEM (EFTEM) and aberration corrected high angle annular dark-field (HAADF) STEM, in combination with atom probe tomography (APT). Experimental observations are supported by first-principles based Monte-Carlo modeling of interface properties and phase separation tendencies between B2-NiAl and $L2_1$-Ni_2TiAl.

2. Methods

2.1. Experimental methods

The alloy with a nominal composition Fe–8.1Al–12.2Cr–1.9Mo–18.2Ni–2.0Ti (in wt.%) (Fe–15.5Al–12.1Cr–1.0Mo–16.0Ni–2.2Ti in at.%) was prepared by arc melting using 99.99% pure elements. Subsequently, ribbons with a width of 2–3 mm and a thickness of 30–50 μm were obtained by the melt-spinning technique, in which the melt was forced through a nozzle with 0.5 mm diameter onto a copper wheel with 200 mm diameter, rotating with a tangential velocity of 30 m/s. The details of the melt-spinning apparatus are described elsewhere [14]. The entire operation was carried out in helium atmosphere. The melt-spun ribbons were aged at 700 °C for 1, 3 and 10 h after encapsulating in an evacuated and sealed quartz tube.

Samples for transmission electron microscopy (TEM) and atom probe tomography (APT) were prepared by Focused Ion Beam (FIB) thinning in a FEI Strata 235 dual beam system. For TEM analysis, a membrane of $10 \times 6 \times 0.5$ μm was cut from the melt-spun ribbons with 30 keV Ga-ions. The membrane was transferred to a Cu-grid and thinned to about 200 nm in thickness with the Ga-ion beam. To minimize effects from ion beam damage and surface oxidation, samples were thinned to electron transparency in a low energy high precision ion mill (Fischione Nanomill) with 900 eV Ar-ions.

Electron diffraction patterns, dark-field images and STEM-EDS elemental maps were acquired in a FEI Titan 80–300 microscope equipped with a ChemiSTEM Si-drift EDS-system operated at 200 and 300 kV. Energy-filtered imaging was performed in a Zeiss Libra200MC microscope with a corrected in-column omega energy filter at 200 kV. Monochromated aberration-corrected high angle annular dark-field (HAADF) STEM images were recorded in the double-aberration corrected TEAM0.5 microscope at the National Center for Electron Microscopy (NCEM), operated at an acceleration voltage of 300 kV. For atomic resolution imaging a probe semi-convergence angle of 17 mrad and an inner semi-collection angle of 53 mrad were used.

APT samples were prepared using a site-specific technique described in detail by Thompson et al. [15]. Here, a wedge with the dimensions of $35 \times 3 \times 8$ μm was cut from the sample heat treated for 1 h at 700 °C. The wedge was transferred *in situ* onto a silicon microtip array with an Omniprobe micromanipulator. The wedge was sliced into 6 segments, which were attached to separate silicon posts for further sharpening. Final tip sharpening was done using 30 keV Ga-ions and beam currents down to 30 pA until a final tip radius of ~25 nm and a tip length of ~200 nm was reached.

Pulsed-laser atom-probe tomography was performed using a LEAP (Local Electrode Atom Probe) 4000X Si-X tomograph (Cameca, Madison, WI) [16,17] at a specimen temperature of 60 K. For pulsed-laser dissection, focused picosecond ultraviolet (UV) laser pulses (wavelength = 355 nm) with a laser beam waist of<5 μm at the e^{-2} diameter were used. An UV laser energy of 30 pJ $pulse^{-1}$, and a pulse repetition rate of 250 kHz were utilized. LEAP tomographic data were analyzed employing IVAS (Integrated Visualization and Analysis Software) version 3.6 (Cameca). The measurement errors for all quantities were calculated based on counting statistics and standard error propagation techniques [18].

2.2. Computational methods

Density functional theory (DFT) as implemented in the VASP software [19,20] was employed for first-principles total energy calculations of bulk phases and supercells containing coherent NiAl/Ni_2TiAl interfaces. The calculations made use of the projector augmented wave (PAW) formalism [21,22], within the Perdew–Burke–Ernzerhof parameterization (PBE) of the generalized gradient approximation (GGA) [23]. For all calculations the energy cutoff for the plane wave basis set was fixed to 450 eV.

To study the phase-separation tendencies within the Ti-containing NiAl-based precipitates, we performed cluster-expansion [24–26] based Monte-Carlo simulations of the underlying bulk and interfacial thermodynamic properties. The B2-based Ni($Al_{1-x}Ti_x$) system can be described as a pseudo-binary system [10] where the Ni-sublattice remains effectively unaltered and order–disorder transitions occur by a redistribution of Al and Ti atoms on the Al/Ti-sublattice of the B2-structure. The cluster-expansion developed here for the Ni($Al_{1-x}Ti_x$) system is constructed using the Alloy Theoretic Automated Toolkit (ATAT) [24], based on first-principles calculations of the ordering energetics as x is varied from 0 to 100 at.%, with the Ni species acting as so-called spectator atoms. Monte-Carlo simulations do not account for elastic contributions to the energy arising from coherency strains between the B2- and $L2_1$-phases.

For all of the structures considered in the construction of the cluster-expansion the geometry of the lattice was constrained to be cubic. Specifically, for each structure the cell volume was first relaxed, with the positions of the atoms and shape constrained to that of a bcc lattice, followed by a relaxation of atomic positions only while constraining the shape of the unit cell to be consistent with the cubic symmetry of the underlying bcc parent lattice. Full relaxations of the cell shape were not permitted, to prevent the system from relaxing to highly distorted structures such as those characteristic of the stable low temperature martensitic phases in the NiAl + Ti system [27,28].

In the cluster-expansion formalism the energy of each atomic configuration can be parameterized in terms of effective cluster interactions multiplied by products of occupation variables (spin variables in the standard Ising model) for given clusters, referred to as cluster correlation functions. Once the effective cluster interactions are obtained, by fitting to the database of first-principles total energy calculations, the energy of each configuration can be directly calculated from the cluster correlation functions. Up to 6th nearest neighbor pair interactions with a maximum interaction radius of 0.7 nm were included to fit the effective cluster interactions to energies obtained by the DFT calculations. The total energies of 171 structures were included in the fit, resulting in a cross-validation score of 6 meV. Phase boundaries between B2-NiAl and $L2_1$-Ni_2TiAl were computed with the cluster-expansion Hamiltonian, using semi-grand canonical Monte-Carlo simulations as implemented in the EMC2 code [25] distributed with the ATAT package [24,25].

Zero-temperature interfacial energies for coherent B2-NiAl/$L2_1$-Ni_2TiAl interphase boundaries were computed by DFT for {100}, {110} and {111} orientations, as follows. For a given periodic supercell geometry containing two {100} interfaces a $14 \times 14 \times 1$ Monkhorst–Pack k-point grid was employed with only one k-point along the long axis of the supercell perpendicular to the interface and 14k-points in each direction within the plane of the interface. The total energy of the cell was obtained by fully relaxing atomic positions and cell shape geometry. Reference total energies for the pure phases were computed using supercells with the same geometry (number of unit cells) as was used for the cells with interfaces. The calculated equilibrium lattice parameter in the plane of the interface, obtained from the relaxation of the interface supercells, was used as a reference lattice parameter for total energy calculations of the pure phases and was fixed to account for the lattice parameter mismatch of B2-NiAl and $L2_1$-Ni_2TiAl. Only the lattice parameter in the direction perpendicular to the interface was optimized for the bulk phases. The same procedure was utilized for the {110} and {111} interface habit planes with k-point grids of $12 \times 16 \times 1$ and $17 \times 17 \times 1$ respectively (where again 1k-point was used in the direction normal to the interfaces). The zero-temperature interfacial energies were obtained from the energy difference between the interface-containing supercells and the concentration-weighted average energy of the strained bulk phases.

Finite-temperature interphase boundary free energies and interface concentration profiles were calculated from the cluster-expansion Hamiltonian, using a separate Monte-Carlo code based on the Metropolis algorithm [29]. Simulations for interface supercells were performed in the canonical ensemble, i.e., with the overall concentration maintained constant. In these simulations, configurations were sampled by randomly exchanging dissimilar atoms in the simulation cell.

The temperature dependent interfacial free energy γ was determined by a thermodynamic integration of the Gibbs–Helmholtz equation in modified form, following the procedure outlined by Woodward et al. [30]. In this formalism the temperature-dependent interfacial free energy is calculated according to the following formula:

$$\gamma(T) \cdot (2A) = \Delta E_0 - T \cdot \int_0^T \frac{\Delta E(T') - \Delta E_0}{T'^2} dT' \qquad (1)$$

where the temperature-dependent excess internal energy ΔE is defined as $\Delta E = 2\Delta E_{l/2} - \Delta E_l$, where $\Delta E_{l/2}$ and ΔE_l are the internal energies of simulation cells with an equal cross section of area A containing two interfaces with $l/2$ and l number of layers perpendicular to the interface, respectively. In Eq. (1) the subscript 0 denotes values at zero temperature. The internal energies of the simulation cells are determined in independent Monte-Carlo runs with an equilibration period of 10,000 Monte-Carlo sweeps (MCS). One Monte-Carlo sweep represents N number of spin exchange attempts, where N is equal to the number of atoms in the simulation cell. The average energy is extracted from the averaging period for another 10,000 MCS. The simulation cells were first equilibrated at 1200 K and then slowly cooled to 0 K with $\Delta T = 10$ K. The excess energy ΔE was fit with a 6th order polynomial, which was used to integrate Eq. (1). Interface profiles were computed by taking 50 independent samples of the simulation cell every 150 MCS after the equilibration period. The interface profiles were then obtained by taking the average composition for each plane parallel to the plane of the interface. To avoid an artificial broadening of the interface width, the profiles from each Monte-Carlo snapshot were shifted so that the inflection point of each profile lies at the same position.

Dynamical effects were explored qualitatively using kinetic-Monte-Carlo (KMC) simulations based on Kawasaki dynamics [31], where only nearest neighbor spins of opposite type are exchanged to simulate diffusive kinetics. Periodic and fixed boundary conditions were employed for the KMC simulations. To prevent domains from interacting with their periodic image during coarsening, the boundaries of the simulation cell were frozen and atoms were not allowed to move across the cell boundaries. No differences for the early stages of phase separation were observed for periodic or fixed boundary conditions. Each of the cells had dimensions of $19.4 \times 19.4 \times 19.4$ nm^3 with 287,496 atoms. Two initial concentrations of 7.5 at.% and 12.5 at.% Ti were chosen to investigate the influence of composition on phase separation. The systems were rapidly quenched from the disordered state to 73, 373, 673 and 973 K for 1000 MCS. The simulation cell was then annealed at 973 K for another 100,000 MCS. The characteristic domain size was determined every 200 MCS during the annealing period. The average domain size was extracted from the first moment of the static, spherically averaged structure factor, following the procedure in Ref. [32].

3. Experimental results

3.1. Chemistry and ordering

The main phases establishing the hierarchical microstructure are the continuous disordered bcc-Fe matrix (A2), coherent primary B2-NiAl (B2) precipitates and the $L2_1$-Ni_2TiAl ($L2_1$) precipitate substructure. Based on the small lattice mismatch of the three phases and the distinct degrees of ordering, electron diffraction and diffraction contrast imaging are ideally suited tools for identifying the degree of order with high spatial resolution. The crystal structures and the corresponding schematic electron diffraction patterns for the [1 0 1] zone axis are given in Fig. 1.

In the disordered A2-Fe (Fig. 1a) phase all atoms are distributed over the bcc lattice sites with equal probability, leading to the fundamental reflections in electron scattering, as depicted in Fig. 1b. In the B2-NiAl intermetallic phase, with space group $Pm\bar{3}m$ the bcc lattice is decomposed into two specific sublattices occupied primarily by Al and Ni atoms respectively (Fig. 1c). The ordered structure can be identified by $\langle 0\,1\,0\rangle$ and $\langle 1\,1\,1\rangle$ superlattice reflections arising from the difference in atomic structure, and hence atomic scattering potential. The Heusler $L2_1$-phase is a ternary compound with space group $Fm\bar{3}m$ and an additional degree of ordering, with three distinct sublattices. The Ni-sublattice is equivalent to that of the B2-structure but the Al-sublattice of B2 is decomposed into Al- and Ti-rich sublattices (Fig. 1e). The additional degree of ordering leads to the formation of $\langle 1\,1\,1\rangle$ and $\langle 1\,3\,1\rangle$ superlattice reflections which are unique to the $L2_1$-structure, as illustrated in Fig. 1f. Based on the small lattice mismatch of the disordered Fe-matrix and the ordered B2-NiAl and $L2_1$-Ni_2TiAl phases, the fundamental reflections are common to all three phases. Because the B2-structure has half the lattice parameter of the $L2_1$-structure, the $\langle 0\,1\,0\rangle$ and $\langle 1\,1\,1\rangle$ superlattice reflections of B2 are equivalent to the $\langle 0\,2\,0\rangle$ and $\langle 2\,2\,2\rangle$ reflections of the $L2_1$-structure.

3.2. Early stages of phase separation

The microstructure in the as-quenched condition and its evolution during subsequent stages of aging for 1, 3 and 10 h at 700 °C was investigated by TEM. The left column of Fig. 2 shows quadrants of experimental [1 0 1] zone axis diffraction patterns indexed with respect to the $L2_1$-structure. Circles in the diffraction patterns indicate the location of the objective aperture. The right column gives a superposition of corresponding two-beam dark-field images taken with $\langle 1\,1\,1\rangle$ and $\langle 2\,2\,2\rangle$ reflections. Regions with the B2-structure light up in red while regions with the $L2_1$-structure are seen in green.

After rapid solidification primary B2-type precipitates with diameters ranging between 10 and 20 nm are embedded in the disordered Fe-matrix as illustrated in Fig. 2b. Subsequent aging for 1 h at 700 °C leads to the formation of nanometer sized $L2_1$-precipitates seen as green regions within the primary B2-particles and as faint $\langle 1\,1\,1\rangle$-reflections in the diffraction pattern. The B2-precipitates display a cuboidal shape with edge length between 25 and 50 nm. The precipitate size of the $L2_1$-substructure is estimated to be ~5 nm, although the exact sizes are difficult to extract since the $L2_1$-precipitates can overlap through the foil thickness.

Further aging for a total of 3 h at 700 °C results in a well-established precipitate substructure of $L2_1$-precipitates within the primary B2-precipitates. The B2-particles have coarsened with an increase in edge length to values ranging between 40 and 100 nm. The $L2_1$-precipitates adopt a plate shaped geometry with a width of 5–10 nm, and an aspect ratio of ~1/5. The orientation of both the bcc-Fe/B2- and B2/$L2_1$-interfaces is cube-on-cube, suggesting a strong effect of coherency stresses on the interface.

After 10 h of aging at 700 °C the hierarchical microstructure is fully developed, as illustrated by the energy-filtered TEM images in Fig. 3. The B2-particle edge length increases to 60–200 nm. The $L2_1$-precipitates remain mostly plate shaped with a size range from 15 to 20 nm. In

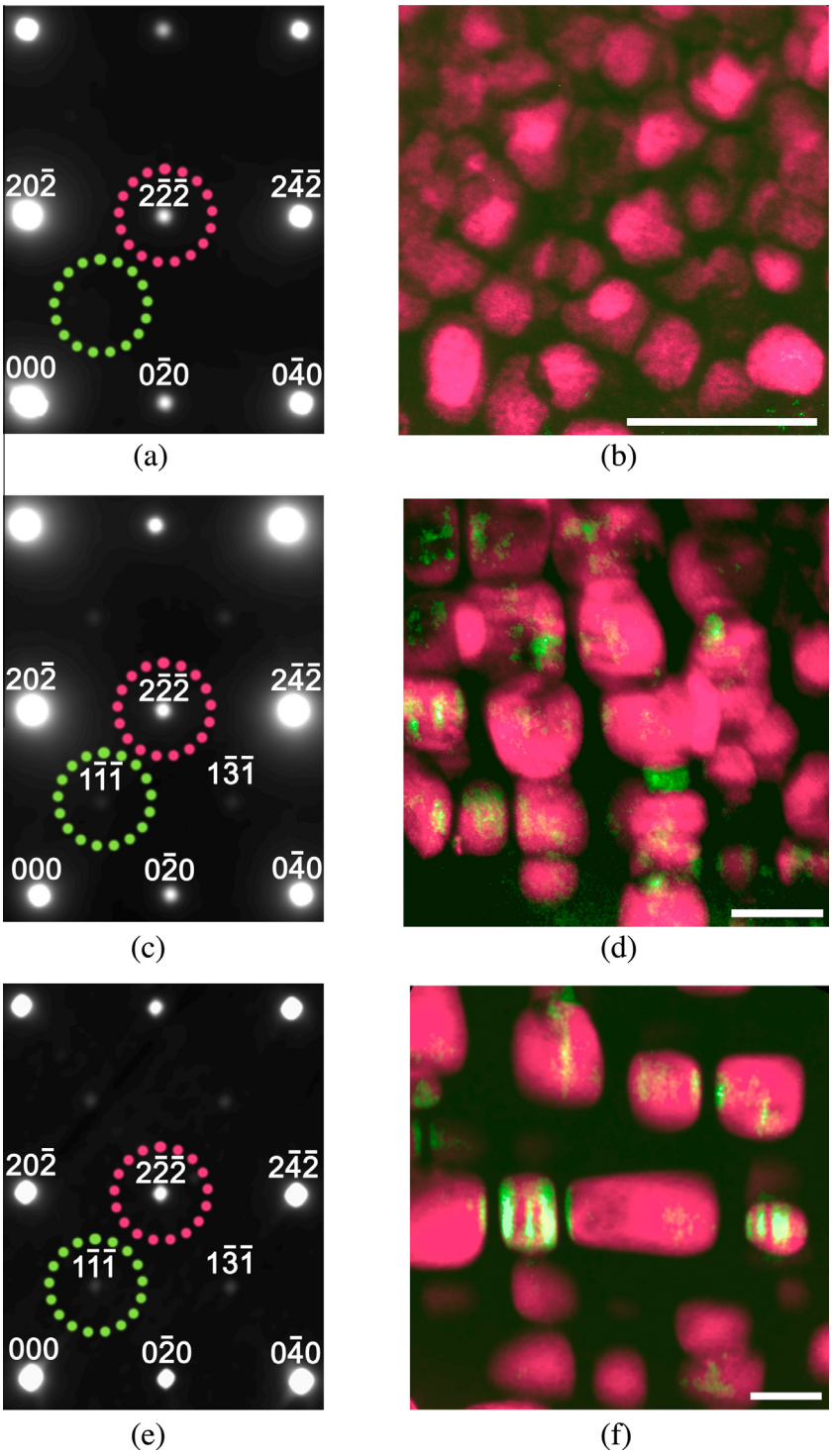

Fig. 2. Series of dark-field TEM images for the alloy in the (a) and (b) as-quenched condition, (c) and (d) after subsequent aging for 1 h at 700 °C and (e) and (f) after subsequent aging for 3 h at 700 °C. The left column shows zone axis diffraction patterns along the [1 0 1] zone axis, the right column composite dark-field images taken with a ⟨1 1 1⟩- and ⟨2 2 2⟩-reflection as indexed with respect to the $L2_1$-crystal structure. The scale bar is 50 nm.

several locations coalescence of precipitates is observed, which in turn can have an impact on the coarsening kinetics [33].

Fig. 4 shows an evolution of elemental partitioning within the precipitates observed after 1 h and 10 h of aging at 700 °C measured by APT and STEM-EDS. To identify the local composition of Ti using APT, the analyzed volume was coarse-grained by forming cubes with 1 nm edge length (voxels). These voxels contain information about the total number of atoms and the atomic fractions of all alloying elements. Thus, the distribution of Ti within the precipitates can be visualized directly.

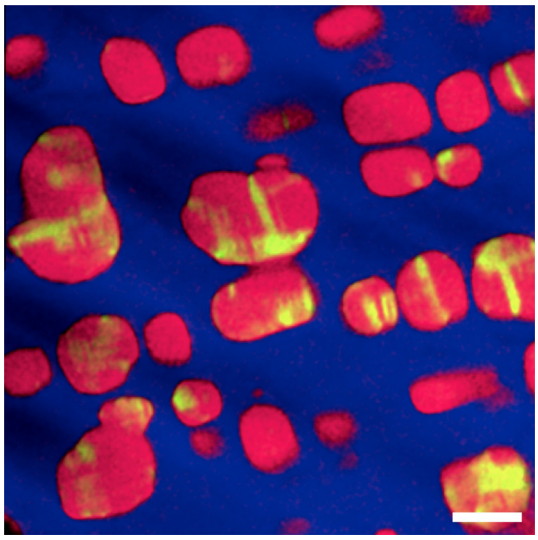

Fig. 3. Core loss energy-filtered TEM images of the Ti-L_{23}, Ni-L_{23} and Fe-L_{23} edges using the three window method and a slit width of 10 eV. The Fe elemental map is shown in blue, Ni in red and Ti in green. The scale bar is 100 nm. (For interpretation of the references to color in this figure legend, the reader is referred to the web version of this article.)

The location of Ti-rich domains with a diameter of<5 nm within the primary B2-precipitates can be resolved by APT and TEM, as shown in Fig. 4a and b. The average Ti concentration, as determined by STEM-EDS and a standardless Cliff–Lorimer correction [34] in the B2-precipitates, is 5 at.%, which is in good agreement with APT measurements of 6 at.%. The Ti-rich regions exhibit Ti levels of 8 at.% as determined by STEM-EDS, and 15 at.% Ti obtained by APT. The difference in measured Ti levels for the small precipitates within the B2-precipitates is based on the fact that the TEM foil thickness is larger than the $L2_1$-precipitate size and hence the B2-phase above and/or below the $L2_1$-precipitates contributes to the X-ray signal. However, Ti concentration modulations and the formation of isolated $L2_1$-precipitates within the B2-precipitates are observed by TEM, STEM-EDS and APT. After aging for 10 h the Ti concentration in the B2-ordered regions remains at 5 at.%, and increases in the developed $L2_1$-precipitates to 12 at.% as determined by STEM-EDS. For both aging conditions 12–13 at.% Fe partitions homogenously to the B2- and $L2_1$-phases within the precipitates.

An aberration-corrected HAADF-STEM image of the B2/$L2_1$ interface in Fig. 4c is shown in Fig. 5. For a better visualization of the differences in ordering the direct nearest neighbor environment of each Ni-sublattice column is colored based on the surrounding intensity difference of neighboring Al, respectively Al and Ti atomic columns (Fig. 5b). The interface between B2 and $L2_1$ is seen to be perfectly coherent, and it shows strong fluctuations in position, extending over several lattice units with an interface width of ~4 nm. At the same time, order–disorder fluctuations are observed within the $L2_1$- and B2-ordered regions at length scales of 1–3 nm.

The differences in ordering between the two intermetallic phases B2 and $L2_1$ can be illustrated by the mean unit cells extracted from the HAADF image of Fig. 5. Here, the intensity of each atomic column of several unit cells is mapped onto a defined unit cell for both phases separately, as shown in Fig. 6a and c for the B2- and $L2_1$-phase. In Fig. 6b and d the corresponding projection of the B2 and $L2_1$ crystal structures are given for comparison. The first obvious observation is that the intensity of the Ni-sublattice columns is equal for both the B2- and $L2_1$-phases, which is consistent with the quasi-binary nature of the B2–$L2_1$ phase equilibria. The Al-columns of the B2-phase have a similar intensity indicating a homogenous distribution of Ti atoms over the Al-sublattice. Every other Al-column is replaced by a Ti-column in the $L2_1$-precipitate as seen in the alternating atomic columns with low (Al) and high (Ti) intensity confirming the higher degree of ordering of $L2_1$.

4. Computational results

4.1. Cluster-expansion

The evolution of the precipitate substructure underlying the hierarchical microstructures described in the previous section is strongly influenced by the B2/$L2_1$ phase equilibria in the pseudobinary Ni($Al_{1-x}Ti_x$) system. A comparison of the relevant phase boundaries in this pseudobinary system calculated by the cluster-expansion [24] with experimental measurements [35–37] is shown in Fig. 7. The predicted phase boundaries are seen to be in good agreement with available experimental data supporting the validity of the cluster-expansion approach employed in this work.

4.2. Interface energies

As a first step in investigating the interface energies relevant for the formation of $L2_1$ from the B2-phase, the 0 K interface energies between B2-structured NiAl and $L2_1$-structured Ni_2TiAl were calculated using DFT. The interface energy γ is defined by $\gamma = (E_{int} - 0.5(E_{B2} + E_{L21}))/2A$. In this relation, E_{int} is the energy of a supercell with two interfaces. E_{B2} and E_{L21} are energies of stoichiometric B2 and $L2_1$ with the same cell geometry as the supercell. The number of layers in between the interfaces was increased to assess convergence with respect to cell size, as illustrated in Fig. 8a. The crystalline anisotropy of the zero-temperature interface energies is characterized by $\gamma_{\{110\}} > \gamma_{\{100\}} > \gamma_{\{111\}}$.

Canonical Monte-Carlo simulations were used to account for the influence of configurational disorder on the finite-temperature interfacial free energies, as described in the Section 2.2. The raw excess energies and polynomial fits are given in Fig. 8b, and the interface free energies derived from Eq. (1) are plotted in Fig. 8c. Low temperature interface energies determined from Monte-Carlo simulations are in good agreement with values obtained by first-principles DFT calculations, in terms of their magnitudes, although the cluster-expansion incorrectly predicts the nature of the crystalline anisotropy. Specifically, while the {1 1 1} interface energy is predicted to be lowest in both the DFT and cluster-expansion results, the latter predicts the wrong ordering of {1 0 0} relative to {1 1 0} (this result is not surprising since the interfacial energies were not included in the fitting of the cluster-expansion). The most important feature of the Monte-Carlo results is that the interfacial energies reduce significantly with increasing temperature, to values on the order of 11 mJ/m^2 at 973 K. At 0 K the cluster-expansion predicts values of the anisotropy ratios of $\gamma_{111}/\gamma_{100} = 0.7$ and $\gamma_{111}/\gamma_{110} = 0.9$. At temperatures representative of the aging temperature of 973 K,

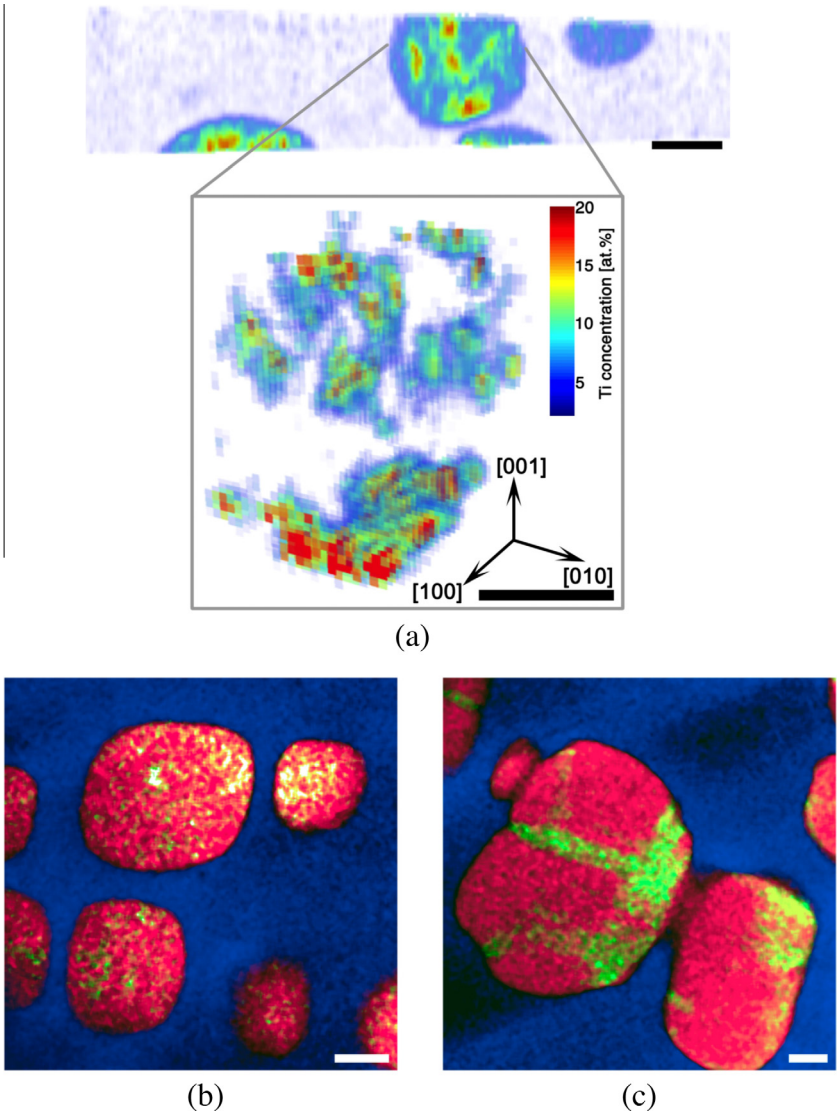

Fig. 4. (a) APT reconstruction of the Ti distribution in $1 \times 1 \times 1$ nm^3 voxels. Upper image gives a larger section from the APT reconstruction of the needle. Lower image shows close up of two-phase precipitate giving the Ti concentration within a B2-precipitate after 1 h of aging at 700 °C. STEM-EDS elemental maps for the alloy determined after (b) 1 h and (c) 10 h of aging at 700 °C. The Fe elemental map is shown in blue, Ni in red and Ti in green. The scale bar is 20 nm. (For interpretation of the references to color in this figure legend, the reader is referred to the web version of this article.)

the anisotropy ratios of $\gamma_{111}/\gamma_{100}$ and $\gamma_{111}/\gamma_{110}$ determined by the cluster-expansion are increased to 1.0 and 1.3 respectively.

Interface concentration profiles were determined by averaging over 50 independent microstates every 150 MCS after equilibration. The {1 0 0} interface adopts a sharp profile at 300 K with a width of ~1 nm as shown in Fig. 9a. At 1000 K the interface width broadens to ~3 nm (Fig. 9b) being consistent with experimental observations reported in the previous section. It can therefore be established that the high temperature state of the interface, including the fluctuations in interface position, was frozen for the experimental samples during air quenching after the aging heat treatment. The agreement between the predicted interface structures and the experimental observations provides an indication that the cluster-expansion based Monte-Carlo simulations capture the main effects on interface structure.

4.3. Kinetic-Monte-Carlo

Kinetic-Monte-Carlo simulations with Kawasaki dynamics were employed to gain further insight into the early stages of the formation of the $L2_1$-phase in the B2-precipitates. As an example, the spherically averaged structure factor for the long wavelength phase separation at the center of the first Brillouin zone and the superlattice reflection of the $L2_1$-phase for a quench to 373 K followed by aging at 973 K is illustrated in Fig. 10.

Ordering of the $L2_1$-phase is observed right after the quench in conjunction with a long wavelength phase separation [38]. This observation establishes that $L2_1$-domains nucleate within the disordered B2-phase and the ordered domains exhibit long wavelength spatial distribution. The growth and coarsening of the ordered $L2_1$-domains is seen in the shift of the peak of the structure factor toward lower

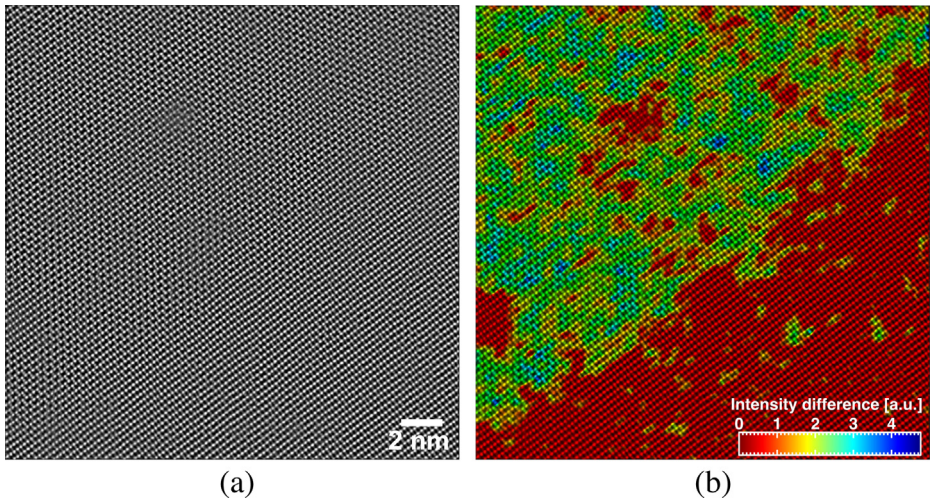

Fig. 5. Aberration-corrected HAADF-STEM image of a B2-$L2_1$ interface in the alloy after aging for 10 h at 700 °C. (a) Shows the Fourier filtered image where a Butterworth filter was used to remove artifacts from surface contamination. (b) For a better visualization of the differences in ordering, the B2- and $L2_1$-sublattice have been colored based on the intensity difference of neighboring Al, respectively Al and Ti atomic columns. Here, red indicates B2- and green $L2_1$-ordering. Perfect B2-order is represented by an intensity difference of 0 and $L2_1$-ordering by intensity differences of >2.5. The corresponding intermediate color values illustrate intermediate stages of ordering between B2 and $L2_1$. (For interpretation of the references to color in this figure legend, the reader is referred to the web version of this article.)

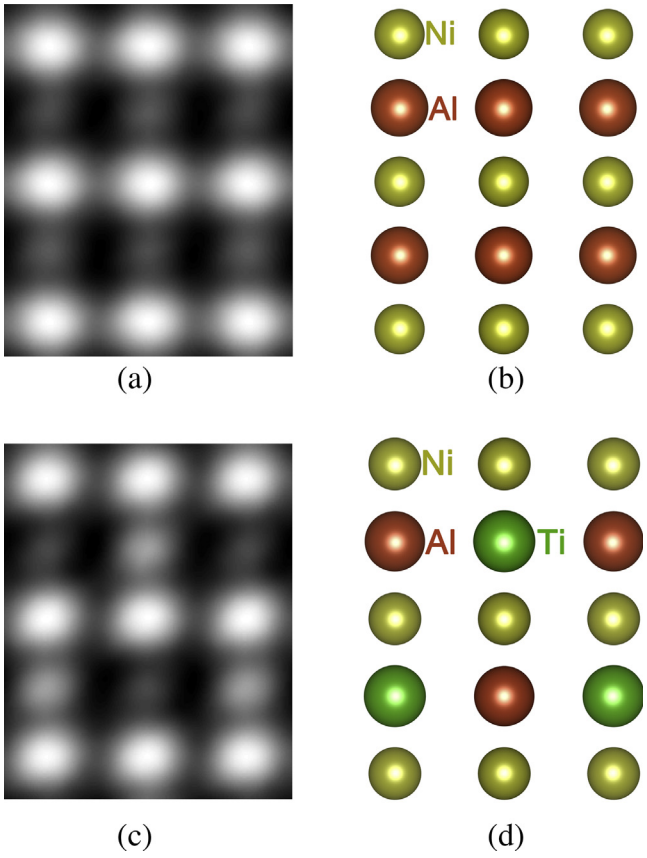

Fig. 6. Experimental mean unit cells of the aberration-corrected HAADF-STEM image of a B2-$L2_1$ interface in [1 0 1] orientation in the alloy after aging at 700 °C for 10 h. (a) Shows the averaged B2 unit cell and (b) the projection of the corresponding B2-crystal structure with indicated atomic column labels. In (c) the average $L2_1$ unit cell is displayed with (d) the projected $L2_1$-crystal structure.

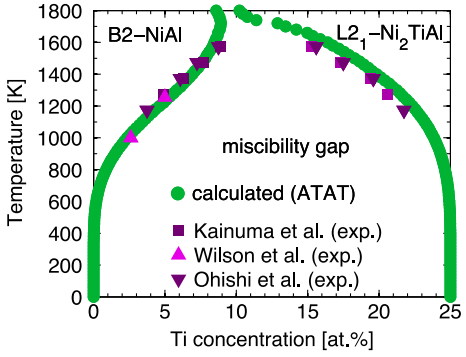

Fig. 7. Calculated phase boundaries of the miscibility gap between B2-NiAl and $L2_1$-Ni_2TiAl in comparison with experimental data.

q-values for the long wavelength phase separation ($q < 0.4\ nm^{-1}$) for the quench and the annealing period. In the early stages of annealing at 973 K, the superlattice reflection sharpens indicating the growth of {1 1 1} ordering waves of the $L2_1$-phase with a wavelength of ~0.51 nm ($q > 1.9\ nm^{-1}$).

Fig. 11 plots the domain size as a function of time for different initial quench temperatures. The initial $L2_1$-domain size is increased with increasing quench temperature observed for times below 1000 MCS during annealing at 973 K, as shown in Fig. 11. In the later stages, domain growth follows a $\sim t^{1/3}$ growth behavior for both concentrations as shown by the solid line in Fig. 11a and e. The domain sizes determined from the spherically averaged structure factor are between 5 and 7 nm after 100,000 MCS. The large scatter can be attributed to the fact that isotropic domains are assumed by spherically averaging the structure factor. However, the forming $L2_1$-domains

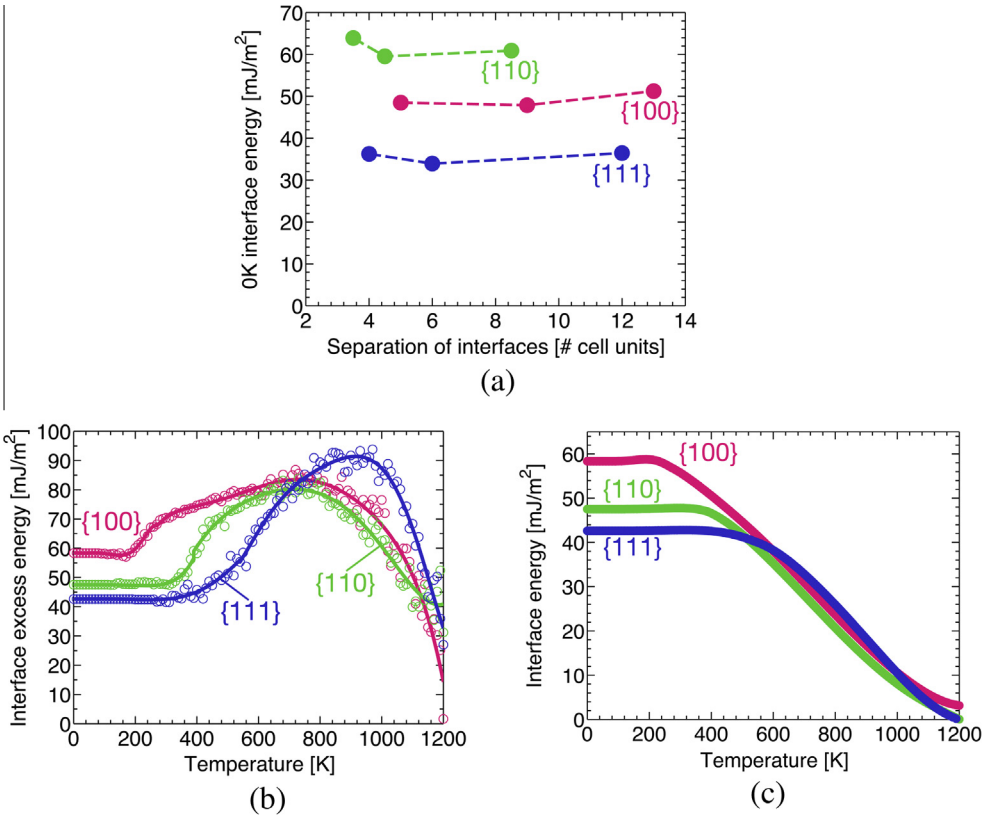

Fig. 8. (a) 0 K interface energies of B2-NiAl and $L2_1$-Ni_2TiAl for the interface habit planes {100} (red), {110} (green) and {111} (blue) calculated from DFT for stoichiometric phases and perfectly sharp interfaces. (b) Excess energy ΔE and polynomial fits from 0 to 1200 K for the {100}, {110} and {111} interface. (c) Gives the temperature dependent interface energy derived through thermodynamic integration between B2-NiAl and $L2_1$-Ni_2TiAl. (For interpretation of the references to color in this figure legend, the reader is referred to the web version of this article.)

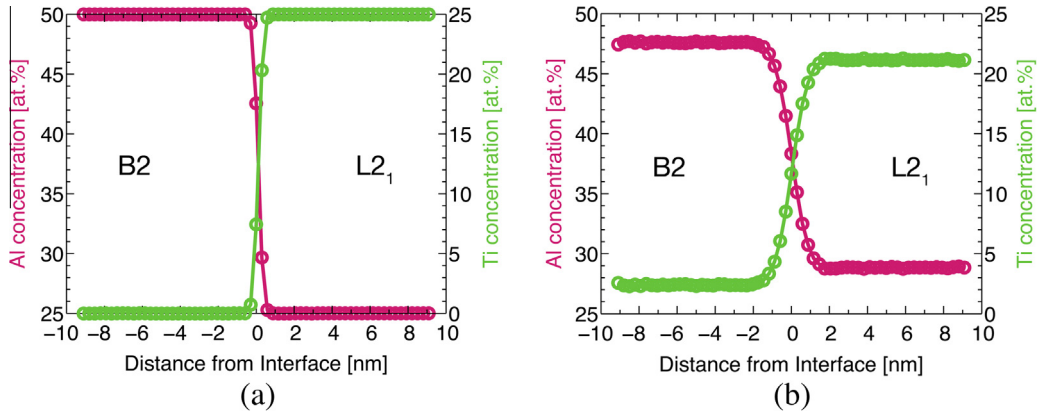

Fig. 9. {100} interface profiles obtained by averaging 50 independent Monte Carlo snapshots after equilibration for (a) 300 K and (b) 1000 K.

exhibit a more ellipsoidal or irregular shape in the final stages of annealing as seen from Fig. 11d and h. The computed $L2_1$ particle shape differs from the experimentally observed plate shaped $L2_1$-precipitates in Section 3.2, because long-range elastic effects are not considered in the Monte-Carlo simulations. However, important material properties governing the morphological evolution of misfitting precipitates are the elastic misfit between matrix and precipitate and the elastic anisotropy of the underlying phases as studied in Ref. [39].

For a concentration of 7.5 at.% Ti (left column in Fig. 11) $L2_1$-domains are forming isolated clusters which coarsen during aging. Inspecting Fig. 11d in more detail reveals that order–disorder fluctuations are observed within the $L2_1$-particles. The B2/$L2_1$ interfaces adopt a rather rough profile due to thermal fluctuations. Both results are in agreement with experimental observations in Fig. 5b.

For a high Ti concentration of 12.5 at.% (right column of Fig. 11) the $L2_1$-domains adopt a more interconnected percolating structure. In the later stages the percolated structure breaks up and separated $L2_1$-domains are observed. The temperature of the initial quench for the conditions investigated here does not have a major impact on the evolving $L2_1$-domains and size, suggesting that slow cooling will lead to a similar microstructure as observed after quenching and annealing.

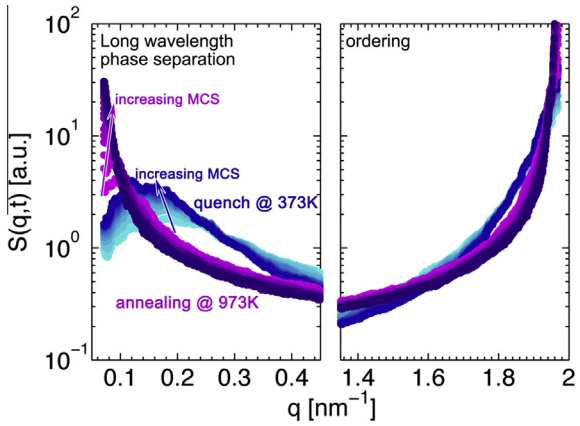

Fig. 10. Spherically averaged structure factor for the center of the first Brillouin zone (left) and for the $L2_1$-superlattice reflection (right). The blue curves represent the structure factor for 100 to 1000 MCS for a quench to 373 K, the purple curves the following anneal at a temperature of 973 K for another 200 to 4000 MCS. (For interpretation of the references to color in this figure legend, the reader is referred to the web version of this article.)

5. Discussion

Microstructure evolution in a ferritic Fe–Al–Cr–Ni based alloy with 2 wt.% Ti additions has been investigated at the nanoscale. In the as-quenched state the microstructure is similar to a typical two-phase precipitation strengthened ferritic alloy without Ti additions [3–8], where B2-NiAl precipitates are coherently embedded in the bcc-Fe matrix. This initial stage represents a microstructure with two levels of hierarchy in both chemical order and length scale. The continuous bcc-Fe matrix is disordered with the main alloying elements being Cr, Ni, Al and Mo. The B2-NiAl precipitates have a size of ~15 nm and are chemically ordered on the bcc lattice with two distinct sublattices. In this early stage the B2-phase is supersaturated with Ti, where it is assumed that Ti atoms occupy the Al-sublattice [40,41]. However, it should be mentioned that the presence of nanometer sized $L2_1$-clusters, as observed by kinetic-Monte-Carlo simulations, cannot be resolved by dark-field imaging and it is well possible that these are already present in the as-quenched condition within the B2-precipitates.

Aging the two-phase quenched microstructure at 700 °C for 1 h leads to the formation of $L2_1$-ordered precipitates within the primary B2-precipitates, establishing a third level of hierarchy both spatially and chemically. The rapid decrease of interfacial energies for temperatures above 350 °C calculated by Monte-Carlo simulations can be expected to facilitate homogeneous nucleation of the $L2_1$-phase from the supersaturated B2-phase, even for rapid cooling conditions [42]. After 3 h of aging at 700 °C the precipitate substructure of $L2_1$-precipitates is well developed and can be clearly distinguished from the surrounding B2-precipitate.

The B2-precipitates and $L2_1$-substructure further grow for aging of 10 h at 700 °C, resulting in an $L2_1$-domain size of ~20 nm. The internal structure of the precipitates and the precipitate composition are similar to B2/$L2_1$-alloys analyzed by Wilson et al. [37]. For such low Ti concentrations no evidence for spinodal ordering was found and the authors state the dominant mechanism for $L2_1$-ordering is homogenous nucleation, which is consistent with the experimental and computational observations in this study. Field et al. [43] however found signs of a spinodal ordering reaction in NiAl/Ni_2TiAl alloys with Ti concentrations ~15 at.%, where B2- and $L2_1$-phases adopt a lamellar microstructure.

The transformation pathway for the alloy studied in the current work is qualitatively different from that observed for ferritic Fe–Al–Cr–Ni based alloys with higher Ti concentration (4 wt.%) in previous work [9]. In the alloy with 4 wt.% Ti the primary precipitate phase formed in the as-quenched condition is $L2_1$, and B2-domains form upon aging by a wetting transition or heterogeneous nucleation on $L2_1$ anti-phase domain boundaries established initially upon solidification and cooling.

In both, the current study and previous work for the alloy with 4 wt.% Ti reported in Ref. [9], the interface between B2- and $L2_1$-phases is observed to be coherent and to have a strong preference for an alignment along {100} planes. This is despite the fact that the calculations presented above show that the interfacial energies are relatively isotropic and display a preference for {110} or {111} facets relative to {100}. It is thus expected that the experimentally observed preference for {100} habits originates from elastic energy, consistent with the analysis presented in Refs. [37,43] for bulk two-phase NiAl–Ni_2TiAl alloys.

Experimentally it is observed that the B2/$L2_1$ interface remains coherent, and pronounced fluctuations of the interface are observed (Fig. 5) leading to a diffuse interface width of ~4 nm. It appears that based on the thin sample geometry the high temperature structure of the interface was preserved after the quench from the aging temperature of 700 °C, as the measured interface widths are in good agreement with the calculated diffuse interface profile obtained by Monte-Carlo simulations near the aging temperature (Figs. 9 and 11). Since the mean square amplitude of the interface fluctuation spectrum is proportional to the inverse of the interface energy [44,45] the computed interfacial energies are a good representation of the experimental observations.

6. Conclusions

This study investigated microstructural evolution in a ferritic Fe–Al–Cr–Ni–Ti based alloy with 2 wt.% Ti additions in the early stages of heat treatment at 700 °C using TEM and APT. First-principles thermodynamic calculations and Monte-Carlo simulations were consistent with experimental observations of interfacial properties and phase decomposition pathways within the primary B2-precipitates. The major conclusions are:

- In the as-quenched state spherical B2-type NiAl precipitates are coherently embedded in the bcc-Fe matrix with diameters ranging between 10 and 20 nm.
- After aging for 1 h at 700 °C the formation of $L2_1$-ordered Ni_2TiAl precipitates below 5 nm in diameter within the primary B2-precipitates is confirmed by TEM and APT measurements.
- The B2-parent precipitate and the $L2_1$-precipitate substructure coarsen in the course of aging for 3 and 10 h. An alignment of the B2/$L2_1$-interface with {100} habit planes is observed and the interface remains coherent throughout the aging heat treatment.

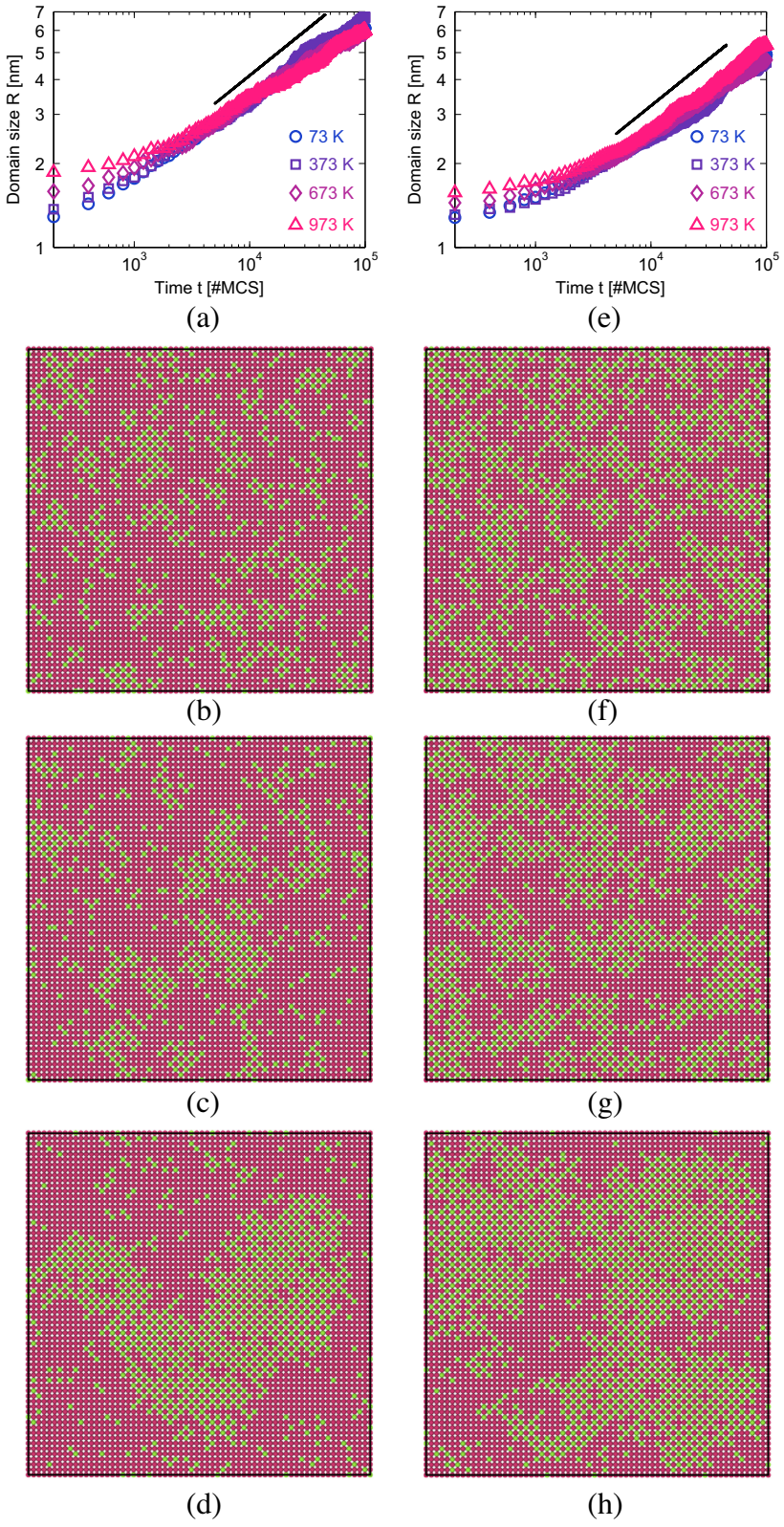

Fig. 11. Average domain size determined from the static, spherically averaged structure factor for a Ti concentration of (a) 7.5 at.% and (b) 12.5 at.%. Cross sections through the simulation cell are given in addition for annealing at 973 K for 200 (b, f), 20,000 (c, g) and 100,000 MCS (d, h). The left column represents data for 7.5 at.% Ti, the right column for 12.5 at.% Ti. Al atoms are shown in red, Ti atoms in green and Ni atoms are not shown for clarity. The projection of the simulation cell is along the [1 0 0] direction. (For interpretation of the references to color in this figure legend, the reader is referred to the web version of this article.)

- After 10 h of aging at 700 °C the interface adopts a diffuse interface profile, consistent with the equilibrium interfacial structure predicted at these temperatures by Monte-Carlo simulations. Order–disorder fluctuations are observed in both B2- and $L2_1$-phases experimentally.
- The calculated 0 K interfacial energies of B2 and $L2_1$ determined by DFT are anisotropic with the order $\gamma_{\{110\}} > \gamma_{\{100\}} > \gamma_{\{111\}}$ and with magnitudes ranging between 30 and 60 mJ/m^2. The $\gamma_{111}/\gamma_{100}$ ratio is 0.7, while that for $\gamma_{111}/\gamma_{110}$ is 0.6.
- The $\gamma_{111}/\gamma_{100}$ ratio of the B2/$L2_1$ interface obtained by Monte-Carlo simulations at 0 K is 0.7, the $\gamma_{111}/\gamma_{110}$ ratio 0.9. The anisotropy ratios increase to $\gamma_{111}/\gamma_{100} = 1.0$ and $\gamma_{111}/\gamma_{110} = 1.3$ at a temperature of 973 K. In addition, the magnitude of the interface free energies reduces from 50 mJ/m^2 at 0 K to 11 mJ/m^2 at 973 K.
- Kinetic-Monte-Carlo simulations confirm the formation of $L2_1$-ordered clusters in the B2-phase after quenching through nucleation. The effect of Ti concentration on the early stages of phase separation is explored, with the main observation being that for a higher Ti level of 12.5 at.%, the $L2_1$-domains exhibit a more interconnected structure in contrast to more isolated clusters for 7.5 at.%. In the late stages of aging order–disorder fluctuations are observed within the $L2_1$-phase and the B2/$L2_1$-interface adopts a rough profile for both concentration levels. These computational results are in agreement with experimental observations.

Acknowledgments

The Electric Power Research Institute (EPRI) under the Grant No. RP8043-1 with Dr. J Stringer as the Grant monitor supported the initial research. The current research is supported by the US Department of Energy (DOE), Office of Fossil Energy, under Grant DE-FE0005868 (Dr V. Cedro, monitor). The authors also gratefully acknowledge the helpful discussions with Prof. P.K. Liaw. Atom probe tomography measurements and analyses were performed at the Northwestern University Center for Atom-Probe Tomography (NUCAPT). Dr. Dieter Isheim's help and suggestions regarding APT sample preparation and data analysis are kindly appreciated. The microscopy work was performed at the National Center for Electron Microscopy (NCEM), which is supported by the Office of Science, Office of Basic Energy Sciences of the US Department of Energy under Contract No. DE-AC02-05CH11231. The authors especially thank Dr. C. Ophus (NCEM) for the assistance in analyzing the high resolution STEM data. The support of the German Research Foundation (DFG) through a research fellowship is highly appreciated by C.H. Liebscher. The initial research had utilized the EPIC facility (NUANCE Center-Northwestern University), which has received support from the MRSEC Program (NSF DMR-1121262) at the Materials Research Center; the Nanoscale Science and Engineering Center (NSF EEC-0647560) at the International Institute for Nanotechnology; and the State of Illinois, through the International Institute for Nanotechnology. We thank Prof. Dr. Helmut Kronmüller for letting us use his melt-spinning facility and Herr Frank Mehner for carrying out melt-spinning experiments at the Max-Planck Institute for Solid State Research (FKF), Stuttgart, Germany. Supercomputing resources were provided by the National Energy Research Scientific Computing Center (NERSC), which is supported by the Office of Science of the US Department of Energy under Contract No. DE-AC02-05CH11231. Additional computational resources were provided by XSEDE (formerly TeraGrid) at the National Center for Supercomputing Applications (NCSA) at the University of Illinois at Urbana-Champaign, IL, the Pittsburgh Supercomputer Center (PSC), Pittsburgh, PA, the San Diego Supercomputer Center (SDSC), San Diego, CA, through the Grant No. DMR070017N, and Northwestern's Quest high performance cluster. VRR acknowledges supports of the Ministry of Education, Science and Technological Development of the Republic of Serbia (Project #172054), and Serbian Academy of Sciences and Arts (Project # F141).

References

[1] Z.K. Teng, F. Zhang, M.K. Miller, C.T. Liu, S. Huang, Y.T. Chou, R.H. Tien, Y.A. Chang, P.K. Liaw, Mater. Lett. 71 (2012) 36.
[2] Z. Sun, C.H. Liebscher, S. Huang, Z. Teng, G. Song, G. Wang, M. Asta, M. Rawlings, M.E. Fine, P.K. Liaw, Scr. Mater. 68 (2013) 384.
[3] N.Q. Vo, C.H. Liebscher, M.J.S. Rawlings, M. Asta, D.C. Dunand, Acta Mater. 71 (2014) 89.
[4] H. Calderon, M.E. Fine, Mater. Sci. Eng. 63 (1984) 197.
[5] H.A. Calderon, M.E. Fine, J.R. Weertman, Metall. Trans. A 19 (1988) 1135.
[6] C. Stallybrass, G. Sauthoff, Mater. Sci. Eng. A 387–389 (2004) 985.
[7] Z.K. Teng, M.K. Miller, G. Ghosh, C.T. Liu, S. Huang, K.F. Russell, M.E. Fine, P.K. Liaw, Scr. Mater. 63 (2010) 61.
[8] Z.K. Teng, C.T. Liu, M.K. Miller, G. Ghosh, E.A. Kenik, S. Huang, P.K. Liaw, Mater. Sci. Eng. A 541 (2012) 22.
[9] C.H. Liebscher, V. Radmilovic, U. Dahmen, M. Asta, G. Ghosh, J. Mater. Sci. 48 (2012) 2067.
[10] B. Burton, J. Osburn, A. Pasturel, Phys. Rev. B Condens. Matter 45 (1992) 7677.
[11] H. Cook, D. De Fontaine, J. Hilliard, Acta Metall. 17 (1969) 765.
[12] D. De Fontaine, Acta Metall. 9 (1975) 553.
[13] D. De Fontaine, J. Appl. Crystallogr. 8 (1975) 81.
[14] I. Bakonyi, F. Mehner, M. Rapp, A. Cziraki, H. Kronmüller, R. Kirchheim, Z. Met. 86 (1995) 619.
[15] K. Thompson, D. Lawrence, D.J. Larson, J.D. Olson, T.F. Kelly, B. Gorman, Ultramicroscopy 107 (2007) 131.
[16] D.N. Seidman, Annu. Rev. Mater. Res. 37 (2007) 127.
[17] T.F. Kelly, M.K. Miller, Rev. Sci. Instrum. 78 (2007) 031101.
[18] L.G. Parratt, Probability and Experimental Errors in Science: An Elementary Survey, John Wiley & Sons, 1961.
[19] G. Kresse, J. Furthmüller, Phys. Rev. B Condens. Matter 54 (1996) 11169.
[20] G. Kresse, J. Furthmüller, Phys. Rev. B 54 (1996) 11169.
[21] P.E. Blöchl, Phys. Rev. B 50 (1994) 953.
[22] G. Kresse, D. Joubert, Phys. Rev. B 59 (1999) 11.
[23] J. Perdew, K. Burke, M. Ernzerhof, Phys. Rev. Lett. 77 (1996) 3865.
[24] A. Van de Walle, M. Asta, G. Ceder, Calphad 26 (2002) 539.
[25] A. Van de Walle, M. Asta, Model. Simul. Mater. Sci. Eng. 0393 (2002) 521.
[26] A. Van de Walle, Calphad 33 (2009) 266.
[27] R. Kainuma, H. Ohtani, K. Ishida, Metall. Mater. Trans. A 27 (1996) 2445.
[28] X. Huang, I. Naumov, K. Rabe, Phys. Rev. B 70 (2004) 064301.
[29] N. Metropolis, A.W. Rosenbluth, M.N. Rosenbluth, A.H. Teller, E. Teller, J. Chem. Phys. 21 (1953) 1087.
[30] C. Woodward, A. van de Walle, M. Asta, D.R. Trinkle, Acta Mater. 75 (2014) 60.
[31] K. Kawasaki, Phys. Rev. 783 (1966) 224.
[32] A. Singh, A. Mukherjee, H.M. Vermeulen, G.T. Barkema, S. Puri, J. Chem. Phys. 134 (2011) 044910.
[33] C. Jayanth, P. Nash, J. Mater. Sci. 24 (1989) 3041.
[34] G. Cliff, G.W. Lorimer, J. Microsc. 103 (1975) 203.
[35] R. Kainuma, K. Urushiyama, K. Ishikawa, C.C. Jia, I. Ohnuma, K. Ishida, Mater. Sci. Eng. A 239–240 (1997) 235.
[36] K. Oh-ishi, Z. Horita, M. Nemoto, Mater. Trans. JIM 38 (1997) 99.

[37] A.W. Wilson, J.M. Howe, A. Garg, R.D. Noebe, Mater. Sci. Eng. A 289 (2000) 162.
[38] W. Soffa, D. Laughlin, in: Proc. an Int. Conf. Solid-Solid Phase Transform, 1982, 159.
[39] M.E. Thompson, C.S. Su, P.W. Vorhees, Acta Metall. 42 (1994) 2107.
[40] A.W. Wilson, J.M. Howe, Scr. Mater. 41 (1999) 327.
[41] A.V. Ponomareva, E.I. Isaev, Y.K. Vekilov, I.A. Abrikosov, Phys. Rev. B 85 (2012) 144117.
[42] K. Russell, Adv. Colloid Interface Sci. 13 (1980) 205.
[43] R. Field, R. Darolia, D. Lahrman, Scr. Metall. 23 (1989) 1469.
[44] J. Hoyt, M. Asta, A. Karma, Phys. Rev. Lett. 86 (2001) 5530.
[45] Y. Mishin, Model. Simul. Mater. Sci. Eng. 22 (2014) 045001.